Optimal Asymmetric Duty Modulation to Minimize Inductor Peak-to-Peak Current for Dual Active Bridge DC–DC Converter

Di Mou, *Student Member, IEEE*, Quanming Luo, *Member, IEEE*, Zhiqing Wang, Jia Li, Yuqi Wei, *Student Member, IEEE*, Haochen Shi, *Student Member, IEEE*, and Xiong Du, *Member, IEEE*

***Abstract*—Asymmetric duty modulation (ADM), as a recently proposed modulation scheme, provides new chance to improve the performance of dual active bridge (DAB) converter. On this basis, an optimal ADM (OADM) scheme is proposed in this article to minimize the inductor peak-to-peak current over the whole voltage and power range. First, the DAB converter adopting ADM scheme is analyzed in frequency-domain and time-domain, and four operating modes are established. Then, the minimum peak-to-peak inductor current for each operating mode is obtained under Karush–Kuhn–Tucker condition, and the corresponding optimal closed-loop control with low calculation complexity is derived. Then, the key values and features of the OADM scheme are compared with recent state of the art, mainly including the inductor root mean square current and soft-switching performance. Finally, an experimental prototype was built to validate the efficiency enhancement of the converter by adopting the proposed OADM scheme.**

***Index Terms*—Asymmetric duty modulation (ADM), dual active bridge (DAB), peak-to-peak current, root-mean-square (rms) current, zero voltage switching (ZVS).**

I. Introduction

In RECENT decades, renewable energy sources have been widely used due to its environment friendly characteristic, and these renewable energy sources play a more and more critical role in relieving the energy crisis and improving the environment. Since both the renewable energy sources [e.g., photovoltaic (PV) cell and fuel cell] and the energy storage devices (e.g., battery pack) are dc sources, dc microgrids are one of the most direct and efficient ways to connect these dc power sources [1], [2]. Fig. 1 shows the typical structure of a residential dc microgrid (RDCMG), which includes the ac grid, renewable energy sources, and storage system, and all of them supply power to the dc bus to meet the requirement of home dc loads. Specially, electric vehicle (EV) can also be regarded as an energy storage system to ensure the stability of the dc-bus voltage. Compared with conventional ac energy systems, the expected advantages of this structure are higher reliability, stability, and efficiency [3].

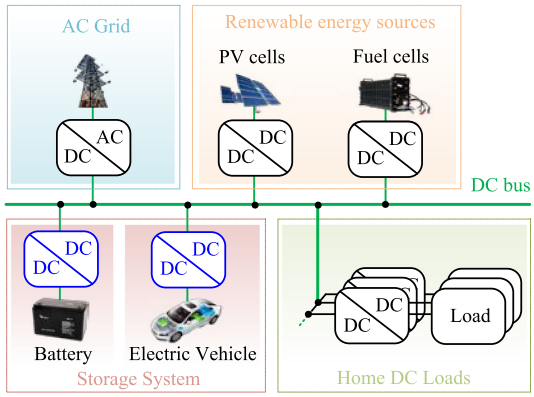

Fig. 1. Structure of RDCMG.

As a controllable converter unit, isolated bidirectional dc–dc (IBDC) converter becomes the essential building blocks for RDCMG. Since the dual active bridge (DAB) converter has many excellent features such as high power density, high efficiency, and low cost with symmetric structure, strong bidirectional power transmission capability, intrinsic soft-switching characteristics, easy modularization, and low component count [4], [5], it is suitable for the RDCMG application to connect dc bus and storage systems.

The conventional modulation scheme for DAB converter is phase-shift modulation (PSM), which controls the direction and magnitude of transmission power by adjusting the phase shift angle between the primary and the secondary bridges [4]–[7], and this angle is called external phase shift angel in this article. Despite the simplicity of PSM, zero voltage switching (ZVS) operation will be lost when the voltages of the dc bus and the storage system do not match well, thus increasing the switching losses. Besides, the large number of reactive power components increases the root-mean-square (rms) value of inductor current,

Manuscript received March 6, 2020; revised May 26, 2020 and July 20, 2020; accepted September 5, 2020. Date of publication September 18, 2020; date of current version November 20, 2020. Recommended for publication by Associate Editor Y. Siwakoti. *(Corresponding author: Quanming Luo.)*

Di Mou, Quanming Luo, Zhiqing Wang, Jia Li, and Xiong Du are with the College of Electrical Engineering, Chongqing University, Chongqing 400044, China (e-mail: dimou428@126.com; lqm394@126.com; 569810311@qq.com; 1374702492@qq.com; duxiong@cqu.edu.cn).

Yuqi Wei is with the Department of, Electrical Engineering,University of Arkansas Fayetteville, Fayetteville, AR 72701 USA (e-mail: 18332550057@163.com).

Haochen Shi is with the Department of Electrical and Electronic Engineering, Xi'an Jiaotong-Liverpool University, Suzhou 215123, China (e-mail: haochen.shi@xjtlu.edu.cn).

Color versions of one or more of the figures in this article are available online at https://ieeexplore.ieee.org.

Digital Object Identifier 10.1109/TPEL.2020.3025120

which results in high conduction loss. As a consequence, its conversion efficiency is reduced, especially at light load.

Accordingly, numerous optimized modulation schemes with more independent modulation variables have been proposed to improve the efficiency of DAB converter [8]–[20]. In addition to the external phase shift angle, the inner bridge phase shift angles in the primary and the secondary bridges are commonly introduced, thus there are at most three independent modulation variables. The recently proposed optimization methods can be mainly classified into the following four categories.

1) *Power-loss-model-based optimization method [13]:* It is the most direct optimization method and can achieve the highest efficiency for all working conditions. However, the loss model has much to do with the hardware parameters, and high efficiency always means high control complexity and low portability.
2) *Reactive power optimization method [14], [15]:* It is also a direct method. However, it is also complicated and the reactive power is difficult to be defined accurately.
3) *ZVS range optimization method [16]:* It optimizes the ZVS performance of each switch as much as possible. However, it may lead to increasing of conduction loss under some operation conditions.
4) *Inductor rms current optimization method [17], [18]:* It is considered as the most effective method to improve the efficiency of DAB converter [12]. However, the ZVS operation cannot be guaranteed for each switch at light load. Specially, the global optimal modulation (GOM) scheme was proposed in [17], which minimizes the inductor rms current over the whole load range, and thus, the conduction loss is greatly reduced. However, there are totally six switches that lose ZVS condition in the low and medium power range, thus leading to high switching loss. Aiming at improving the efficiency, the fundamental duty modulation (FDM) was proposed in [18] based on the fundamental component analysis (FCA) results. Although the ZVS range is extended, the actual inductor rms current is relatively high and can be further optimized since only the fundamental component is considered for the optimization, which leads to great conduction losses, especially at light load.

In conclusion, the above four kinds of methods can truly improve the efficiency of the DAB converter, especially the inductor rms current optimization method. However, they can only reduce the conduction loss and switching loss to some extent. Therefore, the efficiency of DAB converter can be further improved by exploring other schemes. It is noteworthy to mention that a common characteristic for these optimization methods is that the obtained steady-state operating waveforms are symmetrical within half of a switching period and the high-frequency (HF) ac voltages at the primary and secondary sides of the transformer contain two zero-voltage portions within one switching period, thus they belong to symmetric duty modulation (SDM) scheme.

Different from the SDM scheme, the novel asymmetric duty modulation (ADM) scheme with non-50% duty ratio of the switches has been proposed for DAB converter, which can also provide at most three independent modulation variables [8], [19], [20]. The most notable feature of ADM scheme is that the HF ac voltages are composed of two continuous voltage pulses with opposite polarity and each switching period contains only one zero-voltage portion. The authors in [8] combines duty ratios of the primary and secondary half-bridge legs of a dual-active half-bridge converter, and puts forward the scheme of the minimum RMS current of the transformer under the given power. The results show that the proposed modulation scheme has significant efficiency improvement. Besides, a modified minimum current trajectory control method for the dual-bridge series-resonant converter is proposed in [19]. There is only one switch with hard-switching operation in the low and middle power range, and there are two switches that cannot realize ZVS with FDM scheme. This will bring a new perspective that the ADM is better than the SDM in terms of soft-switching performance with the same optimization target. Therefore, it is valuable to explore other optimized ADM schemes for DAB converter. However, ADM also has some inherent problems like the complicated mathematical model of current stress or rms current and the coupling of the variables, which results in nonanalytical optimal solution and difficulties for online calculation. Moreover, since the voltages and currents contain rich even harmonics under ADM scheme, the calculation and optimization results will be inaccurate based on the FCA model.

To solve these problems, in this article, an optimal asymmetric duty modulation (OADM) scheme is proposed, which can further improve the efficiency of DAB converter, especially at light load. For the proposed scheme, the inductor peak-to-peak current is selected as the optimization target, which can also be regarded as the symbol of the rms current to some extent, and the complexity of online calculation is dramatically reduced. Compared with other modulation schemes, the proposed OADM scheme has the following advantages. First, the closed-loop control structure is simpler and the controller needs to be switched only once. Second, the ZVS range of the switches is enlarged significantly, and the current-related losses are reduced.

The rest of this article is organized as follows. In Section II, the operational principles of DAB converter under ADM scheme are introduced and its characteristics are analyzed in frequency-domain. In Section III, the operation modes are established and the steady-state characteristics are deduced in time-domain, especially, the transmission power ranges of different operation modes are established. Based on this, the optimal solutions are derived under the Karush–Kuhn–Tucker (KKT) condition, and the global optimization of the converter under closed-loop control is obtained in Section IV. Then, the key characteristics of PSM, FDM, GOM, and OADM schemes are compared in Section V, which mainly includes the rms current and the soft-switching performance. And the experimental results are presented in Section VI to validate the effectiveness of the proposed scheme. Finally, the conclusion is drawn in Section VII.

II. ADM Scheme

In this section, the topology of DAB converter and the basic operational principles of ADM scheme are introduced. Furthermore, the main characteristics of the converter with ADM are presented by using frequency-domain analysis.

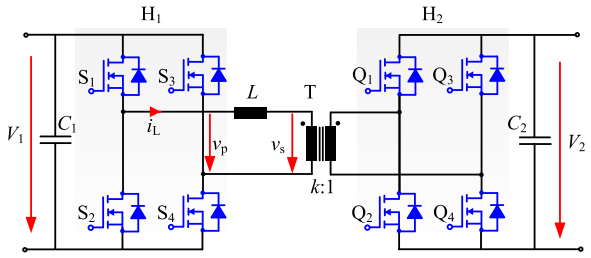

Fig. 2. Schematic of DAB converter.

First, the following assumptions are made.

1) The converter is in steady-state operation.
2) All devices are ideal. Among them, the switches are regarded as an ideal switch with an antiparalleled diode. Besides, the magnetizing current of the transformer is zero.
3) Dead-time intervals between two switching signals of the bridge arm are neglected.

A. Circuit Topology

As depicted in Fig. 2, the DAB converter consists of two H-bridges (H_1 and H_2) assembled by eight switches (S_1–S_4 and Q_1–Q_4), two filter capacitors (C_1 and C_2), an HF transformer T and an equivalent inductor L. The inductor L is composed of the transformer leakage inductor and external auxiliary inductor, which is used as the energy transfer element [18]. In the following analysis, V_1 represents the voltage of the input side, generally connecting to the dc bus, V_2 is the output voltage on the secondary side, generally connecting to the energy storage modules. The transformer turns ratio is N, v_p, and v_s, respectively, represent ac voltages at the primary and secondary side of the HF transformer, i_L is the inductor current, and f_s is the switching frequency.

B. Operational Principle Under ADM Scheme

With ADM scheme, the typical steady-state waveforms of the converter are shown in Fig. 3. There are some restrictions on the gating sequence of the eight switches. Specifically, the switches on one bridge arm are triggered in a complementary manner with non-50% duty ratio. For the primary side switches S_1–S_4, the ON-time for switches S_1 and S_3 (S_2 and S_4) are equal. The ON-time of S_2 and S_4 is no greater than half period, which is defined as D_1T_s. Accordingly, the ON-time of S_1 and S_3 is no less than half period. Similarly, for the secondary side switches Q_1–Q_4, the ON-time of switches Q_1 and Q_3 (Q_2 and Q_4) are equal. The ON-time of Q_2 and Q_4 is no greater than half period, which is defined as D_2T_s, and the ON-time of Q_1 and Q_3 is no less than half period. Besides, there is a phase shift angle D_3 between the turn-ON of S_1 and Q_1. Obviously, both D_1 and D_2 are less than 0.5, while the range of D_3 can be obtained by the following frequency-domain analysis. When D_1 and D_2 equal 0.5, ADM scheme is actually the traditional PSM scheme. In other words, the PSM scheme is a special form of ADM scheme.

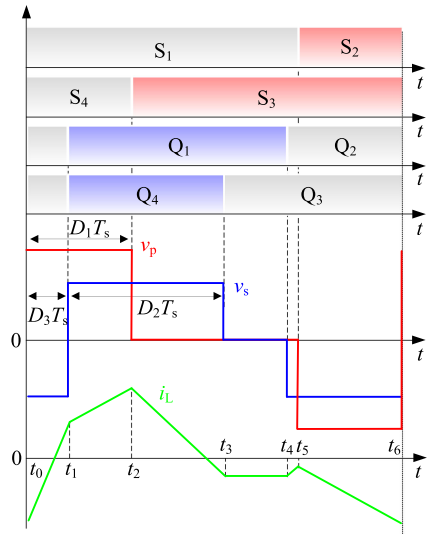

Fig. 3. Typical waveforms of the ADM scheme. From top to bottom are the driving waveforms of eight switches, v_p and v_s, and i_L.

Based on the above analysis, by different combinations of D_1–D_3, different ac voltages v_p and v_s can be obtained, thus leading to different inductor current i_L. Next, by using frequency-domain analysis, the physical meaning of ADM scheme is presented. The expressions of the inductor current and its rms value are obtained to make the comparison among different modulation schemes in Section V.

C. Frequency-Domain Analysis

Theoretically, any periodic functions can be expressed by the infinite series of sine and cosine functions. Therefore, according to Fourier analysis and the circuit characteristics, v_p and v_s can be expressed as

$$\begin{cases} v_p = \sum_{n=1,2,3\ldots}^{\infty} \frac{4V_1}{\pi n} \sin\left(\frac{nD_1\pi}{2}\right)^2 \sin(n\omega t) \\ v_s = \sum_{n=1,2,3\ldots}^{\infty} \frac{4NV_2}{\pi n} \sin\left(\frac{nD_2\pi}{2}\right)^2 \sin\left[n\left(\omega t - D_3\pi\right)\right] \end{cases} \tag{1}$$

where ω is the angular frequency. Then, i_L can be obtained as

$$i_L = \sum_{n=1,2,3\ldots}^{\infty} \frac{4}{n^2\pi\omega L}\left[A(n)\cos(n\omega t) + B(n)\sin(n\omega t)\right] \tag{2}$$

where $A(n)$ and $B(n)$ are

$$\begin{cases} A(n) = NV_2 \sin\left(\frac{nD_2\pi}{2}\right)^2 \cos(nD_3\pi) - V_1 \sin\left(\frac{nD_1\pi}{2}\right)^2 \\ B(n) = NV_2 \sin\left(\frac{nD_2\pi}{2}\right)^2 \sin(nD_3\pi). \end{cases} \tag{3}$$

The output power P can be deduced by multiplying v_p and i_L, which is simplified as

$$P = \sum_{n=1,2,3\ldots}^{\infty} \frac{8NV_1V_2}{n^3\pi^2\omega L} \sin\left(\frac{nD_1\pi}{2}\right)^2 \times \sin\left(\frac{nD_2\pi}{2}\right)^2 \sin(nD_3\pi). \tag{4}$$

It can be seen from (4) that the output power P is composed of odd harmonic components and even harmonic components, which is different from SDM that contains only odd harmonic components. When the converter operates in the forward direction (the power flows from V_1 port to V_2 port), D_3 is required to be greater than zero, and vice versa. To simplify analysis, only the forward mode is discussed in this article.

As mentioned above, the inductor rms current is essential since it relates to the conduction loss. From (2), I_{Lrms} can be deduced as

$$I_{\mathrm{Lrms}} = \frac{2\sqrt{2}}{\pi\omega L}\sqrt{\sum\nolimits_{n=1,2,3\ldots}^{\infty}\left(\frac{1}{n^2}\sqrt{A(n)^2+B(n)^2}\right)^2}. \quad (5)$$

From (3) and (5), the inductor rms current is composed of a superposition of the odd and even harmonic components, and it is determined by $A(n)$ and $B(n)$ directly. For a certain output power, the rms value is expected be as small as possible. From (3), if $NV_2\sin(n\pi D_2/2)^2\cos(n\pi D_3)$ and $V_1\sin(n\pi D_1/2)^2$ have the same sign, $A(n)$ will be much smaller than that with a different sign. Accordingly, from (4) and (5), the rms value can then be reduced when transferring the same power. Thus, the range of D_3 should be limited between 0 and 0.25.

When the output power P and the voltage gain conversion ratio M ($M = NV_1/V_2$) are given, many groups of variables (D_1, D_2, D_3) can meet the requirements. In order to minimize the inductor rms current, it is necessary to find the optimal combination of ($D_{1,\,\mathrm{opt}}$, $D_{2,\,\mathrm{opt}}$, $D_{3,\,\mathrm{opt}}$). In recent research woks, there are two main optimization methods based on the frequency-domain analysis. The first method is based on the FCA model [17], [19], which will reduce the accuracy of the ADM scheme because it contains affluent odd and even harmonics. The second method is to find the optimal combination by considering the higher harmonic components and using intelligent algorithms [15]. The disadvantage is that the lookup table is necessary and it is difficult to realize real-time optimal control of the DAB converter. Therefore, in order to improve the optimizing accuracy and realize real-time control, the time-domain analysis is also performed in the following.

III. Calculation of Steady-State Characteristics

Based on the time domain analysis, in this section, the different operating modes of DAB converter under ADM are obtained, as well as the key operating characteristics, mainly including the inductor peak-to-peak current and output power.

A. Operating Mode Classification

As shown in Fig. 3, the initial time is defined as the moment when switch S_1 is gated-ON. In one switching period, the three-level state waveform of v_{p} changes at the moments of D_1T_{s} and $(1-D_1)T_{\mathrm{s}}$, respectively. Specifically, v_{p} is in a high-level state between 0 and D_1T_{s}, in a zero-level state between D_1T_{s} and $(1-D_1)T_{\mathrm{s}}$, and in a low-level state between $(1-D_1)T_{\mathrm{s}}$ and T_{s}. Similarly, the waveform of v_{s} changes at the moments of $(D_2+D_3)T_{\mathrm{s}}$, D_3T_{s} and $(D_3+1-D_2)T_{\mathrm{s}}$. Therefore, the values of D_1T_{s}, $(1-D_1)T_{\mathrm{s}}$, $(D_2+D_3)T_{\mathrm{s}}$, D_3T_{s} and $(D_3+1-D_2)T_{\mathrm{s}}$ in a switching period determines the operation waveforms, and thus determines the different operating modes. Obviously, $D_1\,T_{\mathrm{s}}$ and D_3T_{s} can only locate in the first half of the period, and $(1-D_1)T_{\mathrm{s}}$ and $(D_3+1-D_2)T_{\mathrm{s}}$ can only locate in the second half of the period. Meanwhile, the $(D_3+1-D_2)T_{\mathrm{s}}$ is indeed greater than $(D_2+D_3)T_{\mathrm{s}}$. In addition, if D_1T_{s} is less than D_3T_{s}, it will bring much reactive power and directly increase inductor rms current according to the experience in the previous SDM scheme [15]. Therefore, this article does not discuss this condition in order to simplify the analysis process. Accordingly, the possible sequence of them can be illustrated in Fig. 4, and there are four operating modes as follows.

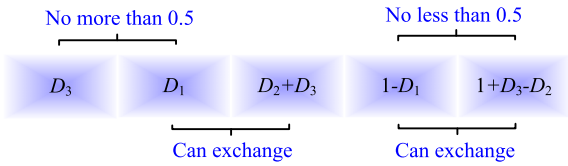

Fig. 4. Possible sequence of D_3, D_1, D_2+D_3, $1-D_1$, $1+D_3-D_2$.

Mode I: The sequence of them in one switching period is D_3T_{s}, D_1T_{s}, $(D_2+D_3)T_{\mathrm{s}}$, $(D_3+1-D_2)T_{\mathrm{s}}$, $(1-D_1)T_{\mathrm{s}}$ from left to right, as depicted in Fig. 5(a). Thus, $D_2-D_3\geq D_1$ should be met in this mode.

Mode II: The sequence of them is D_3T_{s}, D_1T_{s}, $(D_2+D_3)T_{\mathrm{s}}$, $(1-D_1)T_{\mathrm{s}}$, $(D_3+1-D_2)T_{\mathrm{s}}$, as depicted in Fig. 5(b). Thus, $D_1-D_3\leq D_2$, $D_2\leq D_1+D_3$ and $D_2\leq 1-D_1-D_3$ should be met in this mode.

Mode III: The sequence of them is D_3T_{s}, D_1T_{s}, $(1-D_1)T_{\mathrm{s}}$, $(D_2+D_3)T_{\mathrm{s}}$, $(D_3+1-D_2)T_{\mathrm{s}}$, as depicted in Fig. 5(c). Thus, $D_2+D_3\geq 1-D_1$ should be met in this mode.

Mode IV: The sequence of them D_3T_{s}, $(D_2+D_3)T_{\mathrm{s}}$, D_1T_{s}, $(1-D_1)T_{\mathrm{s}}$, $(D_3+1-D_2)T_{\mathrm{s}}$, as depicted in Fig. 5(d). Thus, $D_2+D_3\leq D_1$ should be met in this mode.

As can be noticed, there are certain boundary conditions for all four modes. Next, mode I is taken as an example to calculate the expression of steady-state characteristics.

B. Steady-State Characteristics

In a switching period, the solution is analyzed by a segmented linear calculation method, and the period is divided into six intervals (t_0-t_1), (t_1-t_2), (t_2-t_3), (t_3-t_4), (t_4-t_5), and (t_5-t_6), as shown in Fig. 3. For convenience, all the parameters are converted to the transformer primary side. Nevertheless, due to the different expressions of v_{p} and v_{s} in different intervals, the corresponding expressions of the inductor current are different, which can be derived as

$$i_L(t)=\begin{cases} i_L(t_0)+\frac{V_1+NV_2}{L}(t-t_0)\,t_0\leq t\leq t_1\\ i_L(t_1)+\frac{V_1-NV_2}{L}(t-t_1)\,t_1\leq t\leq t_2\\ i_L(t_2)-\frac{NV_2}{L}(t-t_2)\,t_2\leq t\leq t_3\\ i_L(t_3)\,t_3\leq t\leq t_4\\ i_L(t_4)+\frac{NV_2}{L}(t-t_4)\,t_4\leq t\leq t_5\\ i_L(t_5)-\frac{V_1+NV_2}{L}(t-t_4)\,t_5\leq t\leq t_6. \end{cases} \quad (6)$$

According to the ampere-second balance of the current in a switching period, it can be deduced that the positive area

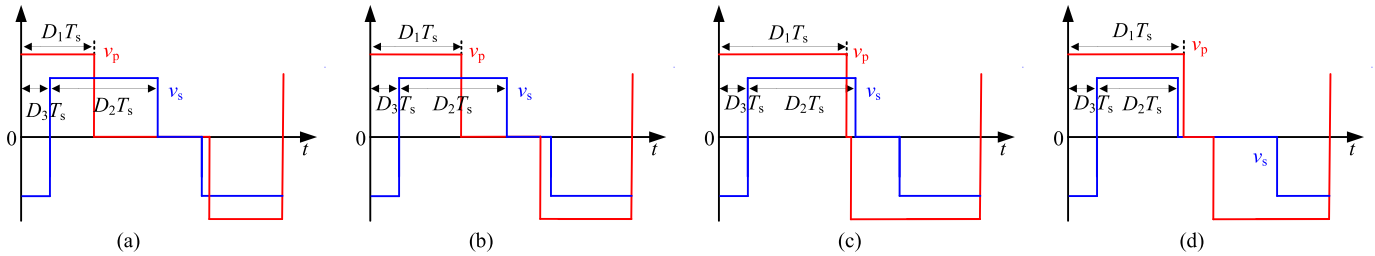

Fig. 5. Classification of ADM scheme modes. (a) Mode I. (b) Mode II. (c) Mode III. (d) Mode IV.

enclosed by the current and the x-axis should be equal to the negative area. Combining with (6), the initial value of the current can be calculated as

$$i_L(t_0) = -\frac{-D_1^2V_1 + D_1V_1 + D_2^2NV_2 - D_2NV_2 + D_3NV_2}{f_sL} = I_{\min}. \tag{7}$$

In mode I, the inductor current reaches its minimum value at t_0, while it reaches its maximum value at t_2, which can be calculated by substituting (7) to (6)

$$i_L(t_2) = \frac{D_1^2V_1 - D_1NV_2 - D_2^2NV_2 + D_2NV_2 + D_3NV_2}{f_sL} = I_{\max}. \tag{8}$$

Then, by subtracting from (8) and (7), the inductor peak-to-peak value can be obtained as

$$I_{\mathrm{p-\!-p}} = \frac{D_1V_1 - D_1NV_2 + 2D_3NV_2}{f_sL}. \tag{9}$$

It can be seen from (9) that the peak-to-peak value is only related to D_1 and D_3. However, the squared term of D_2 is included in (7) and (8), which will increase the calculation complexity when taking $i_{\mathrm{L}}(t_0)$ and $i_{\mathrm{L}}(t_2)$ as the optimization target. As for rms, the current expression is more complicated. Thus, in order to simplify the optimization process, the inductor peak-to-peak current expressed by (9) is selected as the optimization target for the ADM in the following, which is simple and can be regarded as a symbol of rms current under the same output power.

From (6) to (8), the expression of the average output power can be obtained as

$$P = \frac{1}{T}\int_0^T v_p i_L dt = \frac{NV_1V_2}{f_sL} D_3(2D_1 - D_3). \tag{10}$$

According to (9) and (10), the unified output power P' and the unified peak-to-peak current $I'_{\mathrm{p-p}}$ can be deduced as

$$\begin{cases} P' = \frac{P}{P_{\mathrm{b}}} = 2\pi M D_3(2D_1 - D_3) \\ I'_{\mathrm{p-p}} = \frac{I_{\mathrm{p-\!-p}}}{I_{\mathrm{b}}} = 2\pi(D_1 - D_1M + 2D_3M) \end{cases} \tag{11}$$

where I_{b} and P_{b} are defined as

$$\begin{cases} I_{\mathrm{b}} = \frac{V_1}{2\pi f_sL} \\ P_{\mathrm{b}} = \frac{V_1^2}{2\pi f_sL}. \end{cases} \tag{12}$$

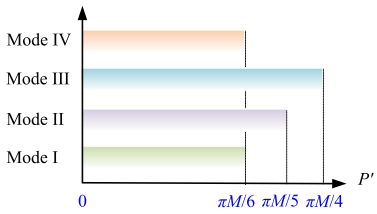

Fig. 6. Range of transmission power in different modes.

The derivation process of P' and $I'_{\mathrm{p-p}}$ for other modes is similar to that of mode I discussed above, and the final results are shown in Table I. Then, it can be seen from Table I that the inductor peak-to-peak current of modes I, II and III are the same, which will facilitate the following optimization. The boundary of each mode operation can be obtained by combining the expression of mode operation constraint and the corresponding transmission power. According to the range of D_1 to D_3 in different modes, the corresponding output power range can be calculated by D_1 to D_3 sequentially. For example, the constraint conditions that D_1 to D_3 should satisfy $D_2 - D_3 \geq D_1$ in mode I. At the same time, D_1, D_2, and D_3 need to meet their boundary conditions, respectively. Then, the transmission power boundary can be obtained by substituting into the expression of the transmission power. Finally, the transmission power range can be derived as 0 to $\pi M/6$. Similarly, the transmission power ranges of other three modes can be deduced, and the results are shown in Fig. 6. The transmission power range of mode IV is 0 to $\pi M/6$, the transmission power range of mode II is 0 to $\pi M/5$, and the transmission power range of mode III is 0 to π $\pi M/4$.

IV. Optimization of Modulation Scheme

In this section, aiming at the minimization of the inductor peak-to-peak current, the optimal path is obtained for each mode. Then, by comparing these paths, the global optimal solution is derived. Generally, this optimization can be expressed as

$$\begin{aligned} &\text{Minimize } I'_{\mathrm{p-p}}(D_1, D_2, D_3) \\ &\text{Subject to } P'(D_1, D_2, D_3) - P^* \leq 0 \\ &\quad h_i(D_1, D_2, D_3) = 0 \, (i = 1, 2, \ldots, n). \end{aligned} \tag{13}$$

In (13), P^* is the given power and h_{i} represents the boundary condition of the control variables. KKT condition is a widely

TABLE I
OUTPUT POWER AND PEAK-TO-PEAK EXPRESSIONS

	Mode operational constraints	Transmission power	Inductor peak-to-peak current
Mode I	$D_2 - D_3 \geq D_1$	$P' = 2\pi M D_3 (2D_1 - D_3)$	$I'_{\text{p-p}} = 2\pi (D_1 - D_1 M + 2D_3 M)$
Mode II	$D_1 - D_3 \leq D_2 \leq D_1 + D_3, D_2 \leq 1 - D_1 - D_3$	$P' = \pi M \left(-D_1^2 + 2D_1 D_2 + 2D_1 D_3 - D_2^2 + 2D_2 D_3 - 3D_3^2\right)$	$I'_{\text{p-p}} = 2\pi (D_1 - D_1 M + 2D_3 M)$
Mode III	$D_3 + D_2 \geq 1 - D_1$	$P' = 2\pi M \left(-D_1^2 + D_1 - D_2^2 + D_2 - 2D_3^2 + D_3 - 0.5\right)$	$I'_{\text{p-p}} = 2\pi (D_1 - D_1 M + 2D_3 M)$
Mode IV	$D_3 + D_2 < D_1$	$P' = 2\pi M D_3 (2D_2 - D_3)$	$I'_{\text{p-p}} = 2\pi (D_1 - D_2 M + 2D_3 M)$

used optimization method to solve extreme optimization problems with equality constraints and inequality constraints. First, the inequality constraints need to be transformed into equality constraints, and the Lagrange function is obtained as

$$L = I'_{\text{p-p}}(D_1, D_2, D_3) + \lambda \cdot P'(D_1, D_2, D_3) + \sum_{i=1}^{m} u_i \cdot h_i(x). \tag{14}$$

In (14), λ is the Lagrange multiplier corresponding to the inequality constraint $P'(D_1, D_2, D_3)$, μ_i is the Lagrange multiplier of equality constraint $h_i(x)$. Then, the KKT conditions are expressed as

$$\begin{cases} \frac{\partial I'_{\text{p-p}}}{\partial D_j} + \lambda \frac{\partial P'}{\partial D_j} + \sum_{i=1}^{n} \mu_j \frac{\partial h_j}{\partial D_j} = 0 \, (j = 1, 2, 3) \\ h_i(D_1, D_2, D_3) = 0 \; u_i g_i(D_1, D_2, D_3) = 0 \; u_i \geq 0 \; \lambda \neq 0. \end{cases} \tag{15}$$

By substituting the expressions of each mode into (13)–(15) and solving them, the optimal solutions for each mode can be obtained, as shown in Table II. It can be seen that except for mode III, the power range is basically divided into two segments. It is noteworthy to mention that modes I and II have the same optimal solution in the first power segment, which indicates that the solutions for these two modes are on the boundary—namely, $D_1 + D_3 = D_2$. Moreover, the whole power range of $(0, \pi M/4)$ is divided into the following five segments: (1)$P' \in (0, \pi M(1 - M^2)/6]$; (2)$P' \in (\pi M(1 - M^2)/6, \pi M(3M + 1)(1 - M)/8]$; (3)$P' \in (\pi M(3M + 1)(1 - M)/8, \pi M/6]$; (4)$P' \in (\pi M/6, \pi M/5]$; (5)$P' \in (\pi M/5, \pi M/4]$. When $P' \in [0, \pi M(1 - M^2)/6]$ and $[\pi M(1 - M^2)/6, \pi M(3M + 1)(1 - M)/8]$, the converter can operate in modes I, II, III or IV; when $P' \in [\pi M/6, \pi M/5]$, it can operate in modes II or III; and when $P' \in [\pi M/5, \pi M/4]$, it can only operate in mode III. For a special power segment, different operation mode commonly means different optimal inductor peak-to-peak current $I'_{\text{p-p}}$, thus it is necessary to decide the operation mode to achieve minimal $I'_{\text{p-p}}$. For the first and second power segments, modes I and II have the same $I'_{\text{p-p}}$, which is lower than that of the other two modes, as shown in Fig. 7(a) and (b). For the third power segment, modes I and II still have the lowest $I'_{\text{p-p}}$, and the value for mode III is quite close to them, as shown in Fig. 7(c). For the fourth power segment, $I'_{\text{p-p}}$ of mode III is lower than that of mode II, as shown in Fig. 7(d). Of course, for the last power segment, the converter operates in mode III as mentioned above. In summary, when $P' \in [0, \pi M(3M + 1)(1 - M)/8]$, which is called low power segment, the converter should operate in mode II, when $P' \in [\pi M(3M + 1)(1 - M)/8, \pi M/4]$, which is called high power segment, it should operate in mode III. Thus, the boundary between them is $P_b{}' = \pi M(3M + 1)(1 - M)/8$, as shown in Fig. 8.

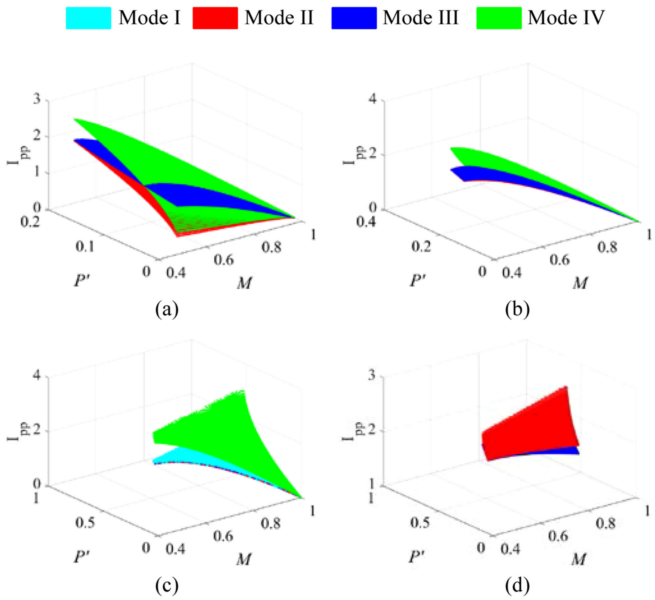

Fig. 7. Comparison of each power segment. (a) $P' \in (0, \pi M(1 - M^2)/6]$. (b) $P' \in (\pi M(1 - M^2)/6, \pi M(3M + 1)(1 - M)/8]$. (c) $P' \in (\pi M(3M + 1)(1 - M)/8, \pi M/6]$. (d) $P' \in (\pi M/6, \pi M/5]$.

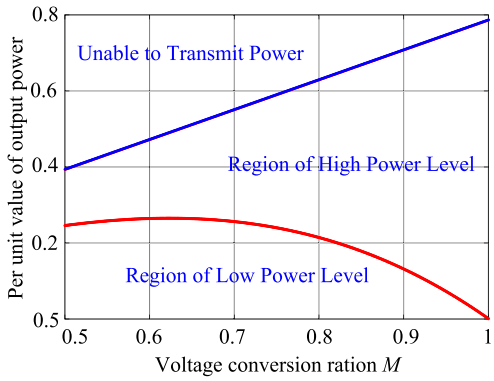

Fig. 8. Low power and high power working range of OADM scheme.

In summary, the optimal solutions for the entire power range only exist in modes II and III, which correspond to low power and

TABLE II
OPTIMAL SOLUTION OF DIFFERENT MODES

	Power Range	Optimal solution
Mode I	$P'\in\left[0,\frac{\pi M(3M+1)(1-M)}{8}\right]$	$D_{1,\text{opt}}=\frac{D_{3,\text{opt}}(M+1)}{(1-M)}, D_{2,\text{opt}}=D_{1,\text{opt}}+D_{3,\text{opt}}$ $D_{3,\text{opt}}=\frac{\sqrt{2\pi}P'\sqrt{\left(-\frac{(3M+1)(M-1)}{MP'}\right)}}{2\pi(1+3M)}$
	$P'\in\left(\frac{\pi M(3M+1)(1-M)}{8},\frac{\pi M}{6}\right]$	$D_{1,\text{opt}}=\frac{1}{2}-D_{3,\text{opt}}, \ D_{2,\text{opt}}=\frac{1}{2}$ $D_{3,\text{opt}}=\frac{1}{6}-\frac{\frac{\pi^{1.5}}{2}(M\pi-6P')\sqrt{\frac{16M}{9\pi M-54P'}}}{4\pi^2M}$
Mode II	$P'\in\left[0,\frac{\pi M(3M+1)(1-M)}{8}\right]$	$D_{1,\text{opt}}=\frac{D_{3,\text{opt}}(M+1)}{(1-M)}, D_{2,\text{opt}}=D_{1,\text{opt}}+D_{3,\text{opt}}$ $D_{3,\text{opt}}=\frac{\sqrt{2\pi}P'\sqrt{\left(-\frac{(3M+1)(M-1)}{MP'}\right)}}{2\pi(1+3M)}$
	$P'\in\left(\frac{\pi M(3M+1)(1-M)}{8},\frac{\pi M}{5}\right]$	$D_{1,\text{opt}}=\frac{2}{5}-\frac{(5D_3-1)(5M-3)}{5(5M-1)}, D_{2,\text{opt}}=\frac{2}{5}-\frac{2(5D_3-1)}{5(5M-1)}$ $D_{3,\text{opt}}=\frac{1}{5}+\frac{\sqrt{2}(5P-\pi M)(5M-1)\sqrt{\frac{15M^2-10M+3}{\pi M^2-5P'M}}}{10\sqrt{\pi}(15M^2-10M+3)}$
Mode III	$P'\in\left[0,\frac{\pi M}{4}\right]$	$D_{1,\text{opt}}=\frac{1}{2}-\frac{1-M}{M}\left(\frac{1}{4}-D_{3,\text{opt}}\right), D_{2,\text{opt}}=\frac{1}{2}$ $D_{3,\text{opt}}=\frac{1}{4}-\frac{\sqrt{2}M(\pi M-4P')\sqrt{\frac{2M-1-3M^2}{M(4P'-\pi M)}}}{4\sqrt{\pi}(3M^2-2M+1)}$
Mode IV	$P'\in\left[0,\frac{\pi M(1-M^2)}{6}\right]$	$D_{1,\text{opt}}=\frac{3}{1-M}D_{3,\text{opt}}, D_{2,\text{opt}}=\frac{M+2}{1-M}D_{3,\text{opt}}$ $D_{3,\text{opt}}=\frac{\sqrt{6}P'}{6\sqrt{\pi}(1+M)}\left[\sqrt{\frac{(1-M)(M+1)}{MP'}}\right]$
	$P'\in\left(\frac{\pi M(1-M^2)}{6},\frac{\pi M}{6}\right]$	$D_{1,\text{opt}}=\frac{1}{2}, \ D_{2,\text{opt}}=\frac{1}{2}-D_{3,\text{opt}}$ $D_{3,\text{opt}}=\frac{1}{6}+\frac{(6P'-M\pi)\sqrt{\frac{M}{\pi M-6P'}}}{6M\sqrt{\pi}}$

high power segment respectively. First, the relationship between D_1, D_2, and D_3 in the low-power segment is

$$\begin{cases} D_{1,\text{opt}}=\frac{D_{3,\text{opt}}(M+1)}{(1-M)}, D_{2,\text{opt}}=D_{1,\text{opt}}+D_{3,\text{opt}} \\ D_{3,\text{opt}}=\frac{\sqrt{2\pi}P'\sqrt{\left(-\frac{(3M+1)(M-1)}{MP'}\right)}}{2\pi(1+3M)}. \end{cases} \tag{16}$$

Then, the relationship between D_1, D_2, and D_3 in the high-power segment is

$$\begin{cases} D_{1,\text{opt}}=\frac{1}{2}-\frac{1-M}{M}\left(\frac{1}{4}-D_{3,\text{opt}}\right), D_{2,\text{opt}}=\frac{1}{2} \\ D_{3,\text{opt}}=\frac{1}{4}-\frac{\sqrt{2}M(\pi M-4P')\sqrt{\frac{2M-1-3M^2}{M(4P'-\pi M)}}}{4\sqrt{\pi}(3M^2-2M+1)}. \end{cases} \tag{17}$$

Actually, there are only two control variables in (16) and (17). In the low power segment, D_1, D_2, and D_3 satisfy the relationship of $D_1+D_3=D_2$. Thus, only D_1 and D_3 need to be determined by the transmission power P and voltage conversion ratio M. In the high-power segment, D_2 remains constant at 0.5. Therefore, only two control variables need to be determined by external conditions.

Based on the abovementioned optimal solution, the proposed OADM scheme is compared with the recently proposed modulation schemes in the following section.

V. COMPARISON OF DIFFERENT MODULATION SCHEMES

In this section, the inductor rms current and the ZVS operation of DAB converter under OADM scheme is compared with the typical modulation schemes of PSM, FDM, and GOM. Then, the control block diagram of the OADM scheme is presented.

A. RMS Current Comparison

The rms current directly determines the conduction loss. In the time-domain analysis, the expression of rms is quite complicated. In this article, the rms value is calculated based on the previous researches with frequency-domain analysis. Then, the

TABLE III
PARAMETERS OF THE DAB CONVERTER

Items	Descriptions	Specifications
V_1	Input Voltage	400 V
V_2	Output Voltage	100–300 V
fs	Switching Frequency	50 kHz
L	Auxiliary Inductor	210 uH
k	Turn Ratio	2:1

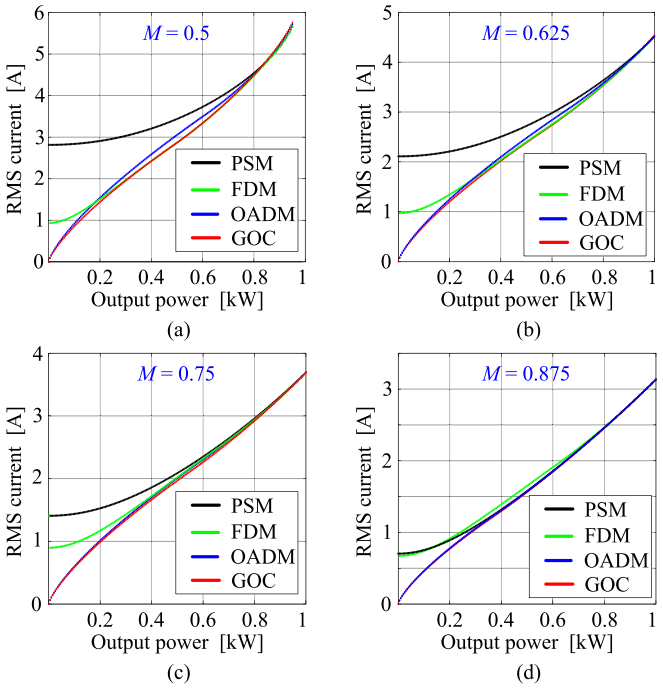

Fig. 9. RMS current of various modulation schemes for (a) $M = 0.5$ V, (b) $M = 0.625$ V, (c) $M = 0.75$ V, (d) $M = 0.875$ V.

complete comparisons of rms values for different modulation schemes under various voltage conversion ratio condition are given in Fig. 9, namely, $M = 0.5$, $M = 0.625$, $M = 0.75$, and $M = 0.875$, which represents that the output voltages $V_2 = 100$V, $V_2 = 125$V, $V_2 = 150$V, and $V_2 = 175$V, respectively. And, the other parameters are shown in Table III.

It can be seen from Fig. 9 that FDM, GOM, and OADM schemes can all reduce inductor rms current significantly, especially at light load. In addition, the inductor rms current obtained by OADM and GOM schemes increase linearly from zero with the increase of power. When $M = 0.625$, $M = 0.75$, and $M = 0.875$, as shown in Fig. 9(b)–(d), OADM and GOM schemes have almost the same inductor rms current. Nevertheless, when $M = 0.5$, the difference between OADM and GOM is a little obvious in the middle power segment, as shown in Fig. 9(a). To summarize, the GOM scheme has the lowest inductor rms current, and the OADM scheme follows, while the other two schemes have higher inductor rms current.

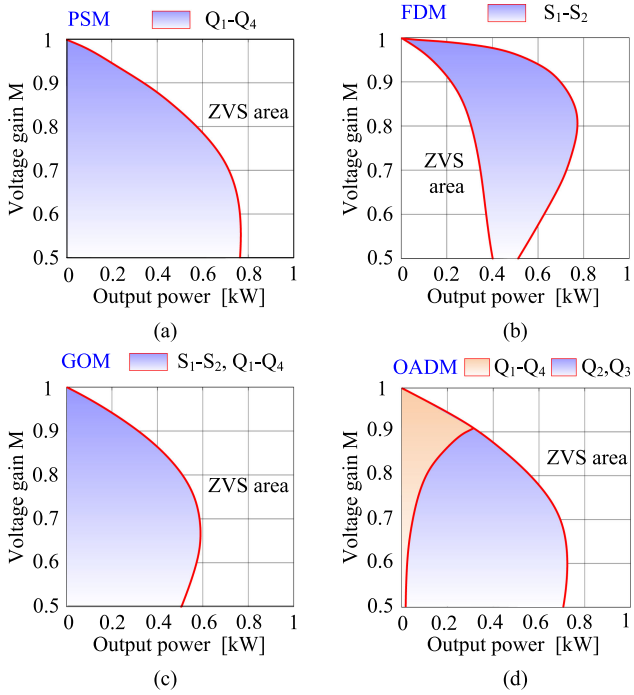

Fig. 10. ZVS performance for different modulation schemes. (a) PSM. (b) FDM. (c) GOM. (d) OADM.

B. ZVS Range Comparison

One of the advantages of the DAB converter is that it can achieve soft-switching operation, which reduces the switching loss and electromagnetic interference [19]. Therefore, the soft-switching performance is a crucial index to evaluate the modulation scheme. To investigate the ZVS boundary of all switches, the inductor current of the moment when switches are gated ON is required [17]. According to the principle of ZVS, the soft-switching boundary conditions are expressed as

$$\begin{cases} \mathrm{S}_1, \mathrm{S}_4 : I_L\left(\omega t = 0\right) \le 0 \\ \mathrm{S}_2 : I_L\left(\omega t = 2\pi D_1\right) \ge 0 \\ \mathrm{S}_3 : I_L\left(\omega t = 2\pi - 2\pi D_1\right) \ge 0 \\ \mathrm{Q}_1, \mathrm{Q}_4 : I_L\left(\omega t = 2\pi D_3\right) \ge 0 \\ \mathrm{Q}_2 : I_L\left(\omega t = 2\pi D_3 + 2\pi - 2\pi D_2\right) \le 0 \\ \mathrm{Q}_3 : I_L\left(\omega \mathrm{t} = 2\pi D_3 + 2\pi D_2\right) \le 0. \end{cases} \tag{18}$$

By substituting (2) into (18), the switch current at turns ON instance can be obtained. Thus, the ZVS conditions can be derived. Similarly, the soft-switching range of other modulation methods can be obtained, then the ZVS performance for various modulation methods is drawn in Fig. 10. Fig. 10 shows the ZVS region with different M over the whole power range. It can be seen that the ZVS range of different modulation schemes vary a lot. For the PSM scheme, there is no phase shift between the bridge arms, so the switches on the primary side and the secondary side are gated-ON and gated-OFF simultaneously. According to the previous analysis, with PSM scheme, the switches on the primary side can realize ZVS, while those on the secondary side perform hard-switching at light load, as shown in Fig. 10(a). For the FDM scheme, the switches S_1 and S_2

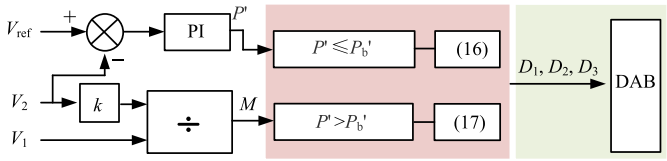

Fig. 11. Block diagram of the voltage-loop controller of the proposed OADM.

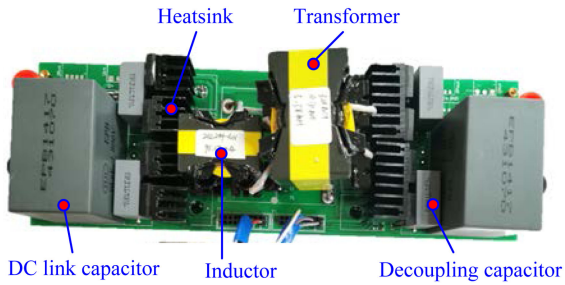

Fig. 12. Experimental prototype.

cannot realize soft-switching in the low and medium power range, as shown in Fig. 10(b), while other switches can realize ZVS. For the GOM scheme, there are six switches that lose ZVS performances in the low and medium power range, as shown in Fig. 10(c). For the OADM scheme, four switches Q_1–Q_4 cannot achieve soft-switching in the yellow area. And Q_2 and Q_3 cannot achieve soft-switching in the low and medium power range. In conclusion, the OADM scheme is better than GOM and PSM in terms of soft-switching performance. However, the ZVS range of this scheme is narrower than that of the FDM scheme.

C. Closed-Loop Control Structure

According to the analysis in Section IV, given the voltage gain and unified power, the control of the OADM scheme can be realized by regulating D_1, D_2, and D_3. The advantages can be summarized as: 1) no additional circuit is needed, thus, the control complexity is reduced; and 2) the traditional proportional integrator (PI) controller is adopted, and the real-time control is achieved. The control block diagram of the OADM scheme is given in Fig. 11. On the one hand, the output voltage V_2 is sensed and compared with the reference voltage $V_{\rm ref}$, after the PI controller, P' is obtained to regulate the output voltage. On the other hand, dividing the output voltage V_2 by the input voltage V_1, the voltage gain M is obtained. It is noteworthy to mention that when M is determined, $P_{\rm b}$' is the unified value under the boundary condition, then, by comparing P' with $P_{\rm b}$', the optimal combination of D_1, D_2, and D_3 can be obtained.

VI. Experiment Verifications

A prototype of the DAB converter in shown Fig. 12, and its technical parameters are summarized in Table III. The specific hardware design is shown in Table IV. The silicon carbide (SiC) MOSFET (SCT2080KE) was selected as the primary and secondary switches of the DAB converter, which has the advantages of low ON-resistance, fast switching speed and simple driving circuit. Finally, extensive experimental results are demonstrated in Figs. 13–15.

TABLE IV
Specific Components

Components	
Switch (S_1-S_4, Q_1-Q_4)	SCT2080KE V_{DSS}=1200V, I_D=40A
Leakage inductor (L)	L=205 uH 25 strands of silk wire (0.1*100) on PQ3535, R_{ac}=80mΩ at 50kHz Material: PC95
Transformer (T)	Pri-26 strands of silk wire (0.1*100), Sec-13 strands of silk wire (0.1*200) on PQ5050, $R_{ac\ (HV)}$=134.55 mΩ, $L_{ac\ (HV)}$=3uH $R_{ac\ (LV)}$=34.25 mΩ, $L_{ac\ (HV)}$=0.78uH Material: PC95
Filter capacitor (C_1, C_2)	EPB 50uF /800V
Control, driving and measurement	
SiC MOSFET drivers	1EDI60N12AF
LV side voltage sensor	AMC1301
Microcontroller	TMS320F28335

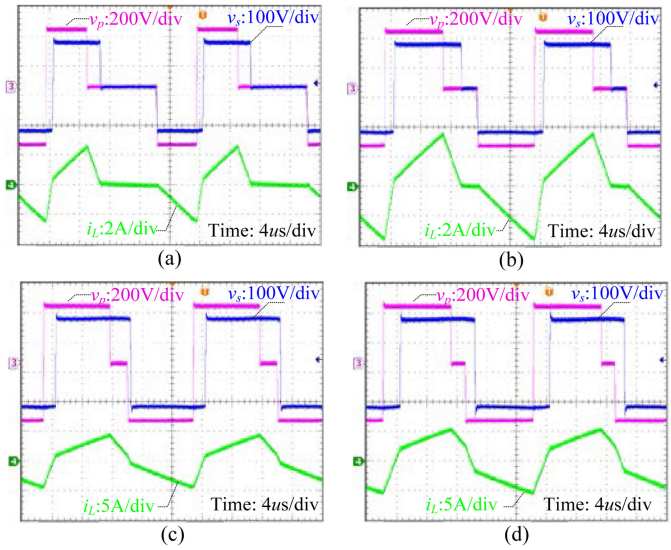

Fig. 13. Experimental waveforms of OADM mode at $V_2 = 150$ V. (a) $P = 250$ W. (b) $P = 500$ W. (c) $P = 750$ W. (d). $P = 1000$ W.

A. Feasibility Analysis of OADM Scheme

In RDCMG, the dc-bus voltage is fixed and the voltage of the storage system is changing. In order to be consistent with the theory analysis above, $V_2 = 100$V, $V_2 = 125$ V, $V_2 = 150$ V, and $V_2 = 175$ V were set in the experimental verification. Fig. 13 shows the steady-state waveforms using the OADM scheme when $V_2 = 150$V. Accordingly, the boundary value between low power and high power segments is $\pi M P_{\rm b}(3M + 1)(1-M)/8 = 580.35$ W based on the theoretical calculation. In Fig. 13(a) and (b), the DAB converter is operated at $P = 250$ W and $P = 500$ W, respectively, both of them work in low power segment. In this mode, the significant feature is $D_1 + D_3 = D_2$, which means switches Q_2 and S_2 are gated-ON at the same

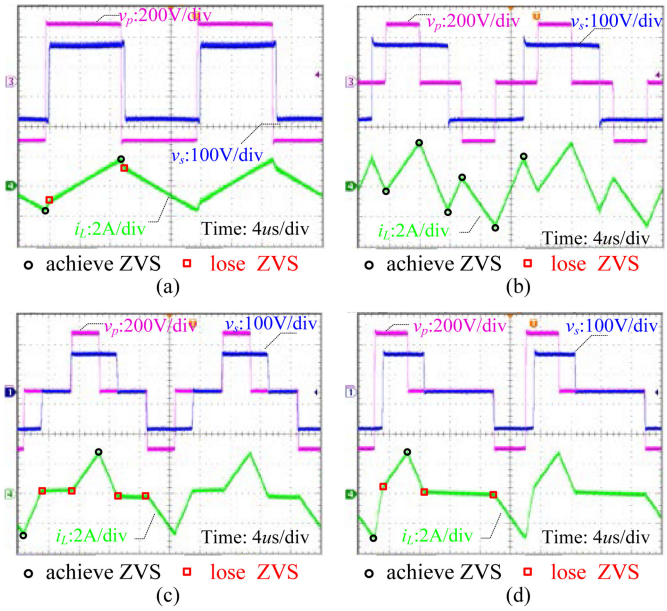

Fig. 14. Experimental waveforms of different modulation modes at $V_2 = 125$ V, $P = 200$ W. (a) PSM. (b). FDM. (c). GOM. (d). OADM.

TABLE V
COMPARISONS OF RMS VALUES UNDER DIFFERENT MODULATION SCHEMES

	RMS value (A)							
	PSM		FDM		GOC		OADM	
	R-v	*T-v*	*R-v*	*T-v*	*R-v*	*T-v*	*R-v*	*T-v*
V_2=100V, P=400W	3.15	3.15	2.41	2.41	2.43	2.43	2.55	2.57
V_2=125V, P=500W	2.71	2.69	2.38	2.39	2.39	2.39	2.47	2.47
V_2=150V, P=200W	1.51	1.50	1.16	1.15	1.02	1	1.02	1
V_2=175V, P=100W	0.74	0.74	0.72	0.73	0.49	0.46	0.49	0.46
V_2=175V, P=700W	2.16	2.15	2.15	2.17	2.14	2.14	2.15	2.15

Notes: *T-v* represents theoretical value; *R-v* represents actual value

time, and the shape of the inductor current eventually appears triangular. In Fig. 13(c) and (d), the DAB converter is operated at $P = 750$ W and $P = 1000$ W, respectively, both of them work in high power segment. All the switches on the secondary side are gated-ON and gated-OFF with a 50% duty cycle in this mode. As can be noticed, the control variables D_1, D_2, and D_3 all move toward to their respective boundaries with the output power increases.

B. Performance Comparison Between OADM and Other Modulation Schemes

For comparison, the DAB converter adopting PSM, FDM, GOM schemes are also tested. Fig. 14 shows the waveforms of these four modulation schemes at $V_2 = 125$ V and $P = 200$ W. From the inductor rms current perspective, for PSM, FDM, GOM, and OADM schemes, the measured values are 2.16, 1.34, 1.21, and 1.24 A, respectively, and the corresponding theoretical values are 2.16, 1.33, 1.2, and 1.24 A. It can be seen that the actual measured values are consistent with the theoretical analysis. Table V randomly gives the comparison of the actual values and

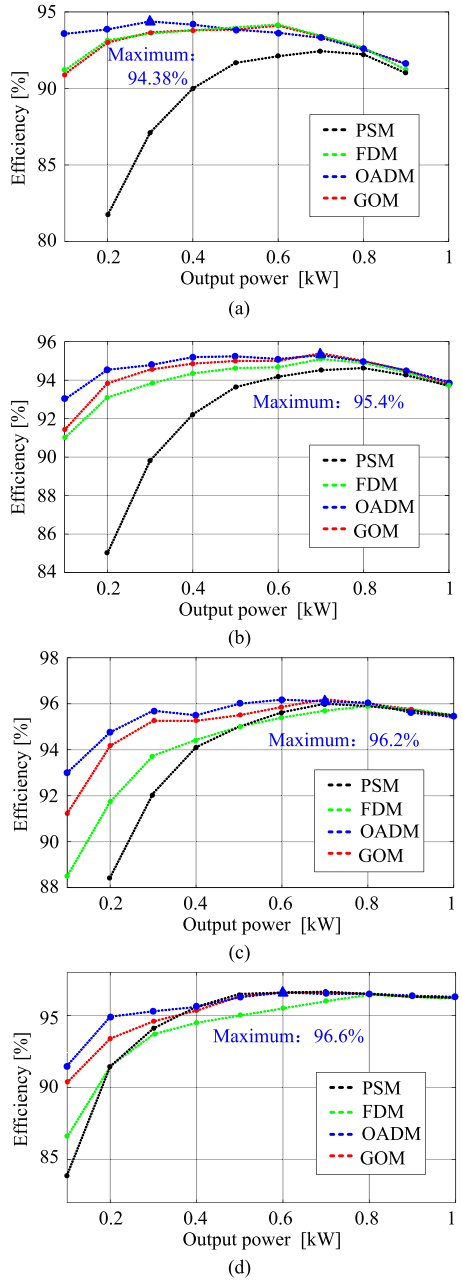

Fig. 15. Experimental efficiency curves of PSM, FDM, GOM, and OADM when voltage conversion ratio M is (a) 0.5, (b) 0.625, (c) 0.75, and (d) 0.875.

the theoretical values of different modulation schemes under several operation conditions, which verifies the correctness of the theoretical analysis. Obviously, FDM, GOM, and OADM have smaller inductor rms current than PSM. Among them, the inductor rms current of FDM is larger than that of GOM and OADM, since only the fundamental component is considered. As could be expected, the inductor rms currents obtained by the OADM and GOM schemes are almost the same.

Then, the four modulation methods are compared in terms of the soft-switching performance. The current and voltage waveforms of the converter with four modulation schemes at $V_2 = 125$V and $P = 200$ W are shown in Fig. 13. It can be seen that they are different under the same conditions, which leads

to different soft-switching performance. In Fig. 13 (a), all the switches on the primary side achieve ZVS, but the switches on the secondary side lose ZVS performance with the PSM scheme. In Fig. 13 (b), all the switches realize ZVS with the FDM scheme. In Fig. 13(c), there are six switches operating under hard-switching condition, which will bring significant turn on loss, but the zero-current switching (ZCS) operation is achieved when they are turned OFF. In Fig. 13(d), three switches realize soft-switching with the OADM scheme, while the switching current of the other five switches (S_2, Q_1–Q_4) are 0.1, 0.09, 0.1, 0.11, 0.09 A, respectively. Among them, the inductor current directions of the switches S_2, Q_1, and Q_4 all meet the necessary conditions, but the energy stored in the junction capacitors is not enough to achieve ZVS. Thus, soft-switching can be partially realized in this case. Based on the above experimental results, it can be concluded that both the inductor current rms value and the soft-switching range are consistent with the theoretical analysis, which verifies the effectiveness of the proposed modulation scheme.

To further present the advantages of the OADM scheme, the efficiency comparison of these four modulation schemes with different voltage conversion ratio is drawn in Fig. 15. It can be concluded that the OADM scheme can almost achieve the highest efficiency over the whole power range with different voltage gains. In addition, as M deviates from 1, the improvement is more obvious, especially at light loads. For example, when $V_2 = 100$ V and $P = 100$ W, the test efficiency of PSM, FDM, GOM, and OADM is 65%, 91.2%, 90.94%, and 93.57%, which is 28.57% higher than traditional PSM and approximately 2.5% higher than GOM and FDM. Therefore, a remarkable performance improvement of the DAB converter can be accomplished by the OADM scheme, especially at light load.

For the DAB converter, the loss mainly includes conduction loss, switching loss, and core loss [17]. The conduction loss is calculated by the rms value of inductor current and the ON-resistance of the switch. The core loss is obtained by the Steinmetz equation with the parameters from the core material datasheet [21]. And the switching loss can be calculated according to the gated-ON and gated-OFF processes. In the end, the loss distribution of the converter under different modulation schemes with different transmission power is obtained, as shown in Fig. 16. The results show that the switching loss accounts for a great proportion of all modulation schemes. Especially, for OADM scheme, its switching loss is the lowest over the whole load range among the four schemes.

C. Transient Response Under the Closed-Loop Control With OADM Scheme

To obtain the transient response performance, the dynamic waveforms when the transmission power changes is given, as shown in Fig. 17. It can be seen that when the power changes from 300 to 750 W, and then from 750 to 300 W, there is no obvious current and voltage overshoot. Moreover, as can be seen from the closed-loop control block in Fig. 11, for both low and high power segments, the output of the PI compensator is compared with the same boundary power, thus, the seamless conversion among different power levels is achieved.

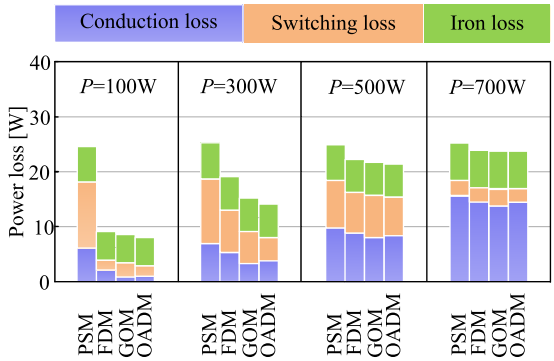

Fig. 16. Loss distribution for PSM, FDM, GOM, and OADM schemes with different transmission power.

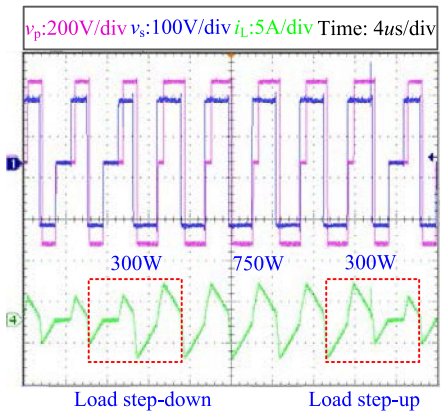

Fig. 17. Dynamic switching waveforms.

VII. Conclusion

This article presents an OADM scheme for the DAB converter, which minimizes the inductor peak-to-peak current with the required transmission power and voltage gain in the whole load range. The ADM scheme, as a recently proposed pulsewidth modulation scheme whose HF ac voltages are composed of two continuous voltage pulses with opposite polarity and each switching period contains only one zero-voltage portion. By comparing the moments when the ac voltage waveform level changes, four operation modes can be established and analytical expressions for converter current and transmission power are derived. After that, to overcome the problems of ADM scheme, like the complex mathematical model of current stress or RMS current as well as coupled variables, the peak-to-peak value of the inductor current is selected as the optimization target, which can also be regarded as the symbol of rms current to some extent, and the complexity of online calculation is dramatically reduced. In the end, an optimal solution was derived under the KKT condition, and the globally optimal closed-loop solution was obtained.

By comparing the recent related works under various operating conditions, we can find that the OADM scheme has certain

advantages according to the soft-switching range and the inductor rms current. Finally, 2.5%–28.57% efficiency improvement for the proposed scheme has been achieved at light load condition compared to the conventional modulation methods. The advantages of the proposed modulation scheme are concluded as follows.

1) The closed-loop control structure is simple and the controller needs to be switched only once.
2) Compared with other modulation schemes, the range of ZVS is enlarged, and the current-related losses are reduced.

In conclusion, the OADM scheme exhibits a good balance between the efficiency and the algorithm complexity.

REFERENCES

[1] A. Chub, D. Vinnikov, R. Kosenko, E. Liivik, and I. Galkin, " Bidirectional DC–DC converter for modular residential battery energy storage systems," *IEEE Trans. Ind. Electron.*, vol. 67, no. 3, pp. 1944–1955, Mar. 2020.

[2] J. Umuhoza, Y. Zhang, S. Zhao, and H. A. Mantooth, " An adaptive control strategy for power balance and the intermittency mitigation in battery-PV energy system at residential DC microgrid level," in *Proc. IEEE Appl. Power Electron. Conf. Expo.*, Tampa, FL, USA, 2017, pp. 1341–1345.

[3] R. M. Burkart and J. W. Kolar, "Comparative η–ρ–σ pareto optimization of Si and SiC multilevel dual-active-bridge topologies with wide input voltage range," *IEEE Trans. Power Electron.*, vol. 32, no. 7, pp. 5258–5270, Jul. 2017.

[4] B. Zhao, Q. Song, W. Liu, and Y. Sun, "Overview of dual-active bridge isolated bidirectional dc–dc converter for high-frequency-link power-conversion system," *IEEE Trans. Power Electron.*, vol. 29, no. 8, pp. 4091–4106, Aug. 2014.

[5] Y. Xie, J. Sun, and J. S. Freudenberg, "Power flow characterization of a bidirectional galvanically isolated high-power dc–dc converter over a wide operating range," *IEEE Trans. Power Electron.*, vol. 25, no. 1, pp. 54–66, Jan. 2010.

[6] D. Costinett, D. Maksimovic, and R. Zane, "Design and control for high efficiency in high step-down dual active bridge converters operating at high switching frequency," *IEEE Trans. Power Electron.*, vol. 28, no. 8, pp. 3931–3940, Aug. 2013.

[7] R. W. A. A. DeDoncker, D. M. Divan, and M. H. Kheraluwala, "A three-phase soft-switched high-power-density dc/dc converter for high power applications," *IEEE Trans. Ind. Appl.*, vol. 27, no. 1, pp. 63–73, Jan./Feb. 1991.

[8] S. Chakraborty and S. Chattopadhyay, "Fully ZVS, minimum RMS current operation of the dual-active half-bridge converter using closed-loop three-degree-of-freedom control," *IEEE Trans. Power Electron.*, vol. 33, no. 12, pp. 10188–10199, Dec. 2018.

[9] D. Costinett, D. Maksimovic, and R. Zane, "Design and control for high efficiency in high step-down dual active bridge converters operating at high switching frequency," *IEEE Trans. Power Electron.*, vol. 28, no. 8, pp. 3931–3940, Aug. 2013.

[10] F. An, W. Song, K. Yang, N. Hou, and J. Ma, "Improved dynamic performance of dual active bridge dc–dc converters using MPC scheme," *IET Power Electron.*, vol. 11, no. 11, pp. 1756–1765, Sep. 2018.

[11] B. Zhao, Q. Song, W. Liu, and W. Sun, "Current-stress-optimized switching strategy of isolated bidirectional DC–DC converter with dual-phase-shift control," *IEEE Trans. Ind. Electron.*, vol. 60, no. 10, pp. 4458–4467, Oct. 2013.

[12] N. Hou and Y. W. Li, "Overview and comparison of modulation and control strategies for a nonresonant single-phase dual-active-bridge DC–DC converter," *IEEE Trans. Power Electron.*, vol. 35, no. 3, pp. 3148–3172, Mar. 2020.

[13] N. Hou, W. Song, Y. Li, Y. Zhu, and Y. Zhu, "A comprehensive optimization control of dual-active-bridge DC–DC converters based on unified-phase-shift and power-balancing scheme," *IEEE Trans. Power Electron.*, vol. 34, no. 1, pp. 826–839, Jan. 2019.

[14] H. Shi, H. Wen, J. Chen, Y. Hu, L. Jiang, and G. Chen, "Minimum-reactive-power scheme of dual-active-bridge DC-DC converter with three-level modulated phase-shift control," *IEEE Trans. Ind. Appl.*, vol. 53, no. 6, pp. 5573–5586, Nov. 2017.

[15] H. Shi, H. Wen, Y. Hu, and L. Jiang, "Reactive power minimization in bidirectional DC-DC converters using a unified-phasor-based particle swarm optimization," *IEEE Trans. Power Electron.*, vol. 33, no. 12, pp. 10990–11006, Dec. 2018.

[16] G. Oggier, G. O. García, and A. R. Oliva, "Modulation strategy to operate the dual active bridge DC-DC converter under soft switching in the whole operating range," *IEEE Trans. Power Electron.*, vol. 26, no. 4, pp. 1228–1236, Apr. 2011.

[17] W. Choi, K. M. Rho, and B. H. Cho, "Fundamental duty modulation of dual-active-bridge converter for wide-range operation," *IEEE Trans. Power Electron.*, vol. 31, no. 6, pp. 4048–4064, Jun. 2016.

[18] A. Tong, L. Hang, G. Li, X. Jiang, and S. Gao, "Modeling and analysis of a dual-active-bridge-isolated bidirectional DC/DC converter to minimize RMS current with whole operating range," *IEEE Trans. Power Electron.*, vol. 33, no. 6, pp. 5302–5316, Jun. 2018.

[19] S. Hu, X. Li, and A. Bhat, "Operation of a bidirectional series-resonant converter with minimized tank current and wide ZVS range," *IEEE Trans. Power Electron.*, vol. 34, no. 1, pp. 904–915, Jan. 2019.

[20] M. Lu, S. Hu, Y. Tang, S. Zhou, and X. Li, "A novel control strategy based on modified gating scheme for a dual-active-bridge converter," in *Proc. 12th IEEE Conf. Ind. Electron. Appl.*, 2017, pp. 1576–1581.

[21] Q. Gu, L. Yuan, J. Nie, J. Sun, and Z. Zhao, "Current stress minimization of dual-active-bridge DC–DC converter within the whole operating range," *IEEE J. Emerg. Sel. Top. Power Electron.*, vol. 7, no. 1, pp. 129–142, Mar. 2019.

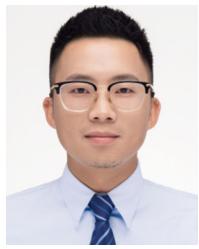

Di Mou (Student Member, IEEE) was born in Lichuan, China, in 1994. He received the B.S. degree in electrical engineering from Three Gorge University, Yichang, China, in 2017. He is currently working toward the Ph.D. degree in electrical engineering with Chongqing University, Chongqing, China.

His current research interests include bidirectional dc–dc converters, electrical vehicles, and power electronic transformers.

Quanming Luo (Member, IEEE) was born in Chongqing, China, in 1976. He received the B.S., M.S., and Ph.D. degrees in electrical engineering from Chongqing University, Chongqing, China, in 1999, 2002, and 2008, respectively.

From 2002 to 2005, he was a Research and Development Engineer with the Emerson Network Power Co. Ltd., Shenzhen, China. Since 2005, he has been with the College of Electrical Engineering, Chongqing University, where he is currently a Professor. He has authored or coauthored more than 40 papers in journal or conference proceedings. His current research interests include LED driving systems, communication power systems, power harmonic suppression, and power conversion systems in electrical vehicles.

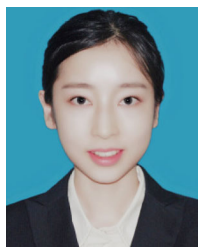

Zhiqing Wang was born in Chongqing, China, in 1994. She received the B.S. and M.S. degrees in electrical engineering from Chongqing University, Chongqing, China, in 2017 and 2020, respectively.

Currently, she is with Monolithic Power Systems, Chengdu, China. Her current research interests include power converter topologies and advanced control for renewable energy systems.

Jia Li was born in Sichuan, China, in 1996. She received the B.S. degree in electrical engineering from Southwest Petroleum University, Xining, China, in 2018. She is currently working toward the Ph.D. degree in electrical engineering with Chongqing University, Chongqing, China.

Her current research interests include bidirectional isolated dc–dc converters, control, and optimization of power electronic systems.

Yuqi Wei (Student Member, IEEE) was born in Henan, China, in 1995. He received the B.S. degree from Yanshan University, Hebei, China, in 2016, the M.S. degree from the University of Wisconsin-Milwaukee (UWM), Milwaukee, WI, USA, in 2018, and M.S. degree from Chongqing University, Chongqing, China, in 2019, all in electrical engineering. He is currently working toward the Ph.D. degree with the University of Arkansas, Fayetteville, AR, USA.

He has authored or coauthored more than 30 peer-reviewed journal and conference papers. His current research interests include topology, modeling and control of dc/dc power converters and power factor correction ac/dc converters, wide band gap devices, and active gate driving.

Mr. Wei serves as a Reviewer for IEEE TRANSACTIONS ON INDUSTRIAL ELECTRONICS, IEEE TRANSACTIONS ON INDUSTRY APPLICATIONS, IEEE ACCESS, and *IET Power Electronics*.

Haochen Shi (Student Member, IEEE) received the B.S. degree from China Three Gorge University, Yichang, China, in 2014, the M.Eng. degree from the University of Leicester, Leicester, U.K., in 2015, and the Ph.D. degree from the University of Liverpool, Liverpool, U.K, in 2020, all in electrical engineering.

Currently, he is a Postdoctoral Fellow with the Huazhong University of Science and Technology, Wuhan, China. His current research interests include bidirectional dc–dc converter, electrical vehicles, and renewable power conversion systems.

Xiong Du (Member, IEEE) received the B.S., M.S., and Ph.D. degrees in electrical engineering from Chongqing University, China, in 2000, 2002, and 2005, respectively.

Since 2002, he has been with Chongqing University, where he is currently a Full Professor with the School of Electrical Engineering. From 2007 to 2008, he was a Visiting Scholar with Rensselaer Polytechnic Institute, Troy, NY, USA. His research interests include power electronics system reliability and stability.

Dr. Du was the recipient of the National Excellent Doctoral Dissertation of China in 2008.